

Boundary Conforming Discontinuous Galerkin Finite Element Approach for Rotorcraft Simulations

O. J. Boelens,* H. van der Ven,[†] and B. Oskam[‡]

National Aerospace Laboratory/NLR, 1006 BM Amsterdam, The Netherlands

and

A. A. Hassan[§]

The Boeing Company, Mesa, Arizona 85215-9797

A numerical method has been developed for predicting the complex vortex wake for a helicopter rotor in hover and in forward flight. The method is based on the solution of the three-dimensional, compressible Euler equations expressed in an arbitrary Lagrangian Eulerian reference frame. A second-order accurate discontinuous Galerkin finite element method is used to discretize the governing equations on a hexahedral mesh. Unstructured, local mesh refinement is performed to enable prediction of the structure of the vortex wake. The capabilities of this computational fluid dynamics method are demonstrated by simulations of the flow around the Caradonna–Tung helicopter rotor in hover and simulations of the flow around the Operational Loads Survey helicopter rotor in forward flight. Accuracy of the method is assessed through comparison with wind-tunnel data, if available. Special attention is given to a rotor trimming procedure developed at the National Aerospace Laboratory/NLR and to the grid adaptation algorithm.

Nomenclature

| | | |
|-------------------|---|-----------------------------------|
| C_{Mx} | = | moment around x axis |
| C_{My} | = | moment around y axis |
| C_p | = | surface pressure coefficient |
| C_T | = | thrust coefficient |
| M | = | local Mach number |
| M_{tip} | = | tip Mach number |
| R | = | rotor tip radius |
| r | = | radial distance along rotor blade |
| x, y, z | = | Cartesian coordinates |
| α_{TPP} | = | tip-path plane angle |
| β_0 | = | collective flap angle |
| β_{1c} | = | cosine-dependent flap angle |
| β_{1s} | = | sine-dependent flap angle |
| $-\Delta C_p M^2$ | = | differential pressure |
| θ | = | pitch angle |
| θ_0 | = | collective pitch angle |
| θ_{1c} | = | cosine-dependent pitch angle |
| θ_{1s} | = | sine-dependent pitch angle |
| μ | = | advance ratio |
| ψ | = | azimuth angle |
| ω | = | vorticity |

Introduction

IT is well known that the prediction of the aerodynamic performance of a helicopter in hover or forward flight is dependent on one's ability to predict accurately its complex vortex wake. To assess the impact of improved airfoil designs, novel blade twist, and

blade planform on rotor performance, it is essential to consider a tool that can accurately predict the rotor wake system. In the following sections, the advantages and limitations of the available rotor flow prediction methods are summarized, with special attention to wake predictions.

Rotor Flow Prediction Methods

The presently available solution techniques for predicting the unsteady aerodynamic response of helicopter rotors can be classified in two categories: 1) vortex-based methods, with a rigidly prescribed wake geometry or with a free wake geometry, and 2) Euler/Navier–Stokes methods. Vortex-based methods have more severe limitations than the more comprehensive Euler/Navier–Stokes methods. The deficiencies of vortex-based methods are related to the additional unknown parameters, for example core size parameters, which have a direct influence on the position and/or motion of the vortex.

In recent years, more comprehensive models that are based on the solution of the Euler and the Navier–Stokes equations (see Refs. 1–20) were developed. The prime objective was to develop solution methods that had minimum reliance on user input while providing the necessary accuracy. In principle, though these formulations are sufficient for capturing the details of the vortical flowfield, excessive numerical diffusion, especially in regions far from the blade, limit their application. To minimize numerical diffusion, researchers embarked on adopting one or more strategies, namely, the use of higher-order numerical schemes,⁹ the use of overset (or chimera) grid systems to resolve the details of the wake away from the blade,^{9,17} and the use of adaptive gridding schemes that are natural for unstructured grid flow solvers.^{1,2,5,6} Among these three strategies, wake capturing through adaptation of an unstructured grid proved to be the most promising, typically, not requiring excessively large grids as with structured grid flow solvers.

State-of-the-Art Flow Solvers for Helicopter Rotors in Forward Flight

In Tables 1 and 2, an overview is given of the present state-of-the-art flow solvers for the simulation of helicopter rotors in forward flight. The discontinuous Galerkin finite element flow solver to be discussed is the only flow solver based on the boundary conforming arbitrary Lagrangian Eulerian (ALE) approach. The other codes apply the chimera or overset approach, where sets of partially overlapping grids are used to cover the computational domain. At the grid overlaps, flow interpolation is required, resulting not only in loss

Presented as Paper 2000-0112 at the 38th Aerospace Sciences Meeting and Exhibit, Reno, NV, 10–13 January 2000; received 28 September 2001; revision received 2 May 2002; accepted for publication 31 July 2002. Copyright © 2002 by the authors. Published by the American Institute of Aeronautics and Astronautics, Inc., with permission. Copies of this paper may be made for personal or internal use, on condition that the copier pay the \$10.00 per-copy fee to the Copyright Clearance Center, Inc., 222 Rosewood Drive, Danvers, MA 01923; include the code 0021-8669/02 \$10.00 in correspondence with the CCC.

*Aerodynamic Research Scientist, Department of Computational Fluid Dynamics and Aeroelasticity, P.O. Box 90502; boelens@nlr.nl.

[†]Mathematical Research Scientist, Department of Mathematical Models and Methods, P.O. Box 90502.

[‡]Division Head, Division of Fluid Dynamics, P.O. Box 90502.

[§]Associate Technical Fellow, McDonnell Aircraft and Missiles Systems.

Table 1 Qualitative comparison of existing rotor codes for forward flight simulation^a

| Code name | Main technique | Flow conservation | Adaptivity | Adaptivity | Accuracy |
|---------------------------|---------------------|-------------------|----------------|----------------|----------|
| ASTRA-OG ^{10,11} | Chimera/overset | Fair | Unsatisfactory | Unsatisfactory | Good |
| FLOWER ¹² | Chimera/overset | Fair | Unsatisfactory | Unsatisfactory | Fair |
| FLOWER ¹³ | Chimera/overset | Fair | Unsatisfactory | Unsatisfactory | Fair |
| OVERFLOW ¹⁶ | Chimera/overset | Fair | Fair | Unsatisfactory | Fair |
| DG flow solver | Boundary conforming | Good | Good | Fair | Good |

^aData is taken from Kondo et al.,¹⁰ Ochi et al.,¹¹ Pahlke,¹² Pahlke et al.,¹³ and Strawn et al.¹⁶

Table 2 Comparison of computing times of existing rotor codes for forward flight simulation

| Code name | Rotor type | Number of blades | Number of grid points ($\times 10^6$) | Computing time for one revolution, h | FLOP count ^a ($\times 10^{12}$) |
|----------------|------------|------------------|---|--------------------------------------|--|
| ASTRA-OG | ATIC AT2 | 5 | 17.0 | 20 on NWT/30 ^b | 1100 |
| FLOWER | OLS | 2 | 1.4 | 107 on Cray J916/1 ^c | 58 |
| FLOWER | ONERA 7AD | 4 | 2.0 | 23.5 on NEC SX-5/1 ^d | 135 |
| OVERFLOW | OLS | 2 | 1.8 | 15 on Cray C-90/1 ^e | 16 |
| DG flow solver | OLS | 2 | 1.2 | 20 on NEC SX-5/8 ^d | 1150 |

^aEstimated from computing times and assumed sustained performance of 30% on vector processor.

^bNumerical Wind Tunnel, parallel vector machine, 1.7 giga FLOP/s peak for processor.

^cParallel vector machine, 0.5 giga FLOP/s peak per processor.

^dParallel vector machine, 8 giga FLOP/s peak per processor.

^eParallel vector machine, 1 giga FLOP/s peak per processor.

of the conservative property, but also increasing the computational costs significantly. Loss of the conservative property is a major concern for the accuracy of the flow solver, and may result in dissipation of vorticity. Ochi et al.¹¹ and Pahlke¹³ report that on parallel vector machines 20% of the computing time is spent in the flow data exchange between the different grids. Moreover, the use of overlapping grids involves a large amount of communication, which reduces the scalability of the chimera or overset approach. Correlating the accuracy of the methods and the required floating point operations (FLOP) count shows that the simulation of a rotor in forward flight is a petaFLOP problem for state-of-the-art algorithms. Hence, acceptable turnaround times can only be accomplished on massively parallel computers or by applying newly developed, more efficient algorithms.

Outline

In this paper, the unique features and the accuracy of a new unstructured flow solver for capturing the wake of helicopter rotors are demonstrated.

First, the features of the discontinuous Galerkin (DG) finite element method are outlined. Next, the rotor trimming procedure for helicopter rotors in forward flight as employed at National Aerospace Laboratory/NLR (NLR) will be presented. Also a section will be dedicated to the grid-adaptation strategy used in the described simulations. Following these discussions, the simulation capabilities of the present computational fluid dynamics (CFD) method for rotorcraft flows are demonstrated using the results of simulations of the flow around the Caradonna–Tung helicopter rotor in hover²¹ and the flow around the Operational Loads Survey helicopter rotor in forward flight. The results of these simulations will be compared with experimental data, if available. A review and conclusions complete the report.

CFD Algorithm

DG Method

The flow solver is based on a DG finite element discretization of the unsteady compressible Euler equations.^{22–24} DG finite element methods use a discontinuous function space to approximate the exact solution of the Euler equations. The DG finite element method is a mixture of a finite element and an upwind finite volume method. The flow domain is discretized into a large number of hexahedral elements. The polynomial expansions of the flowfield variables are purely element based, and there will be, in general, a discontinuity

in the flowfield variables across element faces, with as magnitude the truncation error in the polynomial representation. This discontinuity at element faces is interpreted as a one-dimensional Riemann problem, which is used to obtain a unique definition of element face fluxes. The use of a Riemann problem in the flux calculations has a significant effect in that it introduces upwinding into the finite element discretization. A short introduction to these DG methods is provided in Ref. 22.

Unique Features

A unique feature of the present second-order accurate DG finite element method is that equations are solved not only for the traditional five mean flowfield variables, but also for their spatial gradients. This results in a very compact scheme because it is not necessary to reconstruct the flowfield gradients, necessary to achieve second-order accuracy, using data in neighboring elements. The present finite element method has shock-capturing capabilities and is easy to parallelize because there is limited communication between neighboring elements. The local character of the present finite element method is also beneficial for grid adaptation, which is carried out using anisotropic grid refinement.

The DG finite element method has an inherent ability to handle adaptivity strategies because the refining and derefining of the grid is done without taking into account the continuity restrictions of conventional CFD methods.^{24–27} Note that in the present research h refinement is utilized to construct an isotropic grid from an anisotropic, initial grid. The anisotropy (elements having large aspect ratios) of the initial grid is often a concomitant feature of efficient, boundary-conforming structured grids.

Dynamic motions of multiple moving bodies are simulated using a single, deforming, boundary-conforming mesh. The Euler equations on such a mesh are discretized simultaneously in space and time, leading to an ALE formulation, which incorporates the grid velocities in the flux formulation. Consequently, a conservative scheme that has the same accuracy as the standard DG method for a rigid mesh is obtained. In addition to the governing equations used to evaluate the flowfield gradients in space, equations are also solved for the flowfield temporal gradients. A clear advantage of this solution method is manifest in its ability to use nonuniform time steps without sacrificing temporal accuracy. For unsteady rotor computations, for example, for a rotor in forward flight, this feature can be used to reduce the overall required CPU time (number of azimuthal steps) for the computation of a rotor revolution. This efficiency, of

course, is achieved at the expense of increased memory requirement due to the additional equations being solved for the temporal derivatives of the flowfield variables. The equations are solved implicitly by introducing a pseudotime and marching the solution to a steady state using a standard FAS multigrid scheme. In this way, the ALE method using a single deforming mesh retains the excellent parallelizability properties of the explicit DG method on rigid meshes.

Rotor Trimming

A fair comparison between experimental data and numerical simulations can only be obtained if for both cases the helicopter rotor is operating at the same thrust coefficient. Because the experimental thrust coefficient is fixed, the thrust coefficient obtained during the simulations has to be adjusted in such a way that it matches the experimental one. This adjustment or trimming procedure means that the pitch, flap, and lead-lag schedule are modified in such a way that the thrust coefficient equals the desired value and that both rotor plane moment coefficients are zero.

For a helicopter rotor, the pitch schedule is given by

$$\theta = \theta_0 + \theta_{1c} \cos \psi + \theta_{1s} \sin \psi$$

where ψ is the azimuth angle. Note that during the simulation of the Operational Loads Survey (OLS) helicopter rotor in forward flight the flap schedule has not been modified and that no lead-lag schedule has been used.

The revolution-averaged thrust coefficient C_T and rotor plane moment coefficients C_{Mx} and C_{My} then depend on the collective pitch angle θ_0 , the cosine-dependent pitch angle θ_{1c} , and the sine-dependent pitch angle θ_{1s} .

The revolution-averaged thrust coefficient C_T mainly depends on the collective pitch angle θ_0 , the revolution-averaged moment coefficient around the y axis mainly depends on the cosine-dependent pitch angle θ_{1c} , and the revolution-averaged moment coefficient around the x axis mainly depends on the sine-dependent pitch angle θ_{1s} . Note that the x axis points from the rotor to the tail-rotor and that the y axis points right looking from the tail-rotor to the rotor (pilot's view). The effect of adjusting the rotor collective and cyclic pitch on the thrust coefficient and rotor plane moment coefficients follows from taking the linear term of the Taylor expansion of these equations, that is,

$$\begin{pmatrix} C_T \\ C_{My} \\ C_{Mx} \end{pmatrix} (\theta_0 + \Delta\theta_0, \theta_{1c} + \Delta\theta_{1c}, \theta_{1s} + \Delta\theta_{1s}) \approx \begin{pmatrix} C_T \\ C_{My} \\ C_{Mx} \end{pmatrix} (\theta_0, \theta_{1c}, \theta_{1s}) + \begin{bmatrix} \frac{\partial C_T}{\partial \theta_0} & \frac{\partial C_T}{\partial \theta_{1c}} & \frac{\partial C_T}{\partial \theta_{1s}} \\ \frac{\partial C_{My}}{\partial \theta_0} & \frac{\partial C_{My}}{\partial \theta_{1c}} & \frac{\partial C_{My}}{\partial \theta_{1s}} \\ \frac{\partial C_{Mx}}{\partial \theta_0} & \frac{\partial C_{Mx}}{\partial \theta_{1c}} & \frac{\partial C_{Mx}}{\partial \theta_{1s}} \end{bmatrix} (\theta_0, \theta_{1c}, \theta_{1s}) \begin{pmatrix} \Delta\theta_0 \\ \Delta\theta_{1c} \\ \Delta\theta_{1s} \end{pmatrix}$$

where $\Delta\theta_0$, $\Delta\theta_{1c}$, and $\Delta\theta_{1s}$ indicate the small changes in the collective, cosine-dependent, and sine-dependent cyclic pitch, respectively. The coefficients in the matrix are the sensitivities of the thrust coefficient and rotor plane moment coefficients to changes in the collective and cyclic pitch, with the diagonal terms being the dominant ones.

Because trim simulations are computationally intensive for Euler/Navier–Stokes-based methods, a lifting line vortex method (CAMRAD/JA²⁸) has been used as a first estimate to calculate the sensitivities. The lifting line vortex method, however, only supplies the sensitivities of the thrust coefficient. To obtain the complete sensitivity matrix enabling the proper trimming of the helicopter rotor,

three additional simulations with small variations (order one degree) of either the collective pitch, the cosine-dependent cyclic pitch, or the sine-dependent cyclic pitch are performed with the Euler-based DG method. These simulations start from a periodic solution and are continued until the new solution also is periodic. For the simulation of the OLS helicopter rotor in forward flight, the simulations consisted of one revolution due to the small transient (only a quarter of a revolution). The second-half of this revolution has been used to obtain the forces needed for the sensitivity calculation.

Grid Adaptation

The general idea behind grid adaptation is that, to minimize the numerical diffusion of the vorticity and the numerical dissipation in a vortex, the grid within the vortex should be as isotropic, as uniform, and as refined as possible.

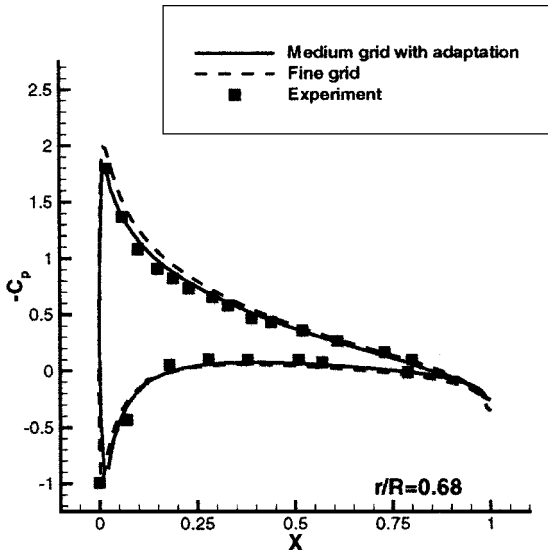
The grid-adaptation algorithm consists of the following parts: First is the grid-adaptation sensor. Basically, two types of sensors are available: 1) sensors that measure differences of flow quantities across element faces and 2) sensors that measure the magnitude of a flow variable in an element. An example of the first sensor type is the standard shock sensor, which measures flow gradients (actually differences) of the five conserved variables and the total pressure loss across element faces. An example of the second sensor type is the vortex sensor based on, for example, the vorticity magnitude. In addition to these sensors one can also use a grid quality sensor, that is, a sensor that measures the jump in the mesh width in the direction normal to the element face, an anisotropy sensor, that is, a sensor that measures the anisotropy (aspect ratios) of an element, and a uniformity sensor, that is, a sensor that measures the mesh width in each coordinate direction.

Second is the grid-adaptation type. The two basic types of grid adaptation are isotropic and anisotropic grid adaptation. If a sensor contains directional information (such as the shock sensor), anisotropic grid adaptation is used. The element is adapted in the direction associated with the gradient. If a sensor contains no directional information, isotropic refinement is used.

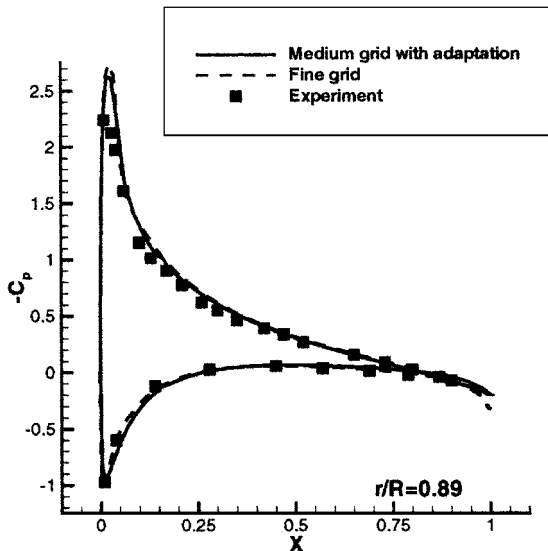
The third is the grid-adaptation control. The adaptation control determines, for example, the adaptation frequency and the percentage of elements that will be removed or refined.

For the helicopter rotor in hover simulations discussed in the next section, the vortex sensor based on the vorticity magnitude ($|\omega|$) is used, combined with a uniformity sensor, resulting in uniform meshes of specified widths (typically 0.005 rotor diameters, i.e., 2.5 times the required width reported by Caradonna²⁹) in the vortex. The grid-adaptation sensor used in the forward flight simulation was a combination of the vortex sensor based on the vorticity magnitude with the anisotropy sensor or the uniformity sensor, resulting once more in uniform meshes of specified width (typically 0.005 rotor diameters) in the vortex.

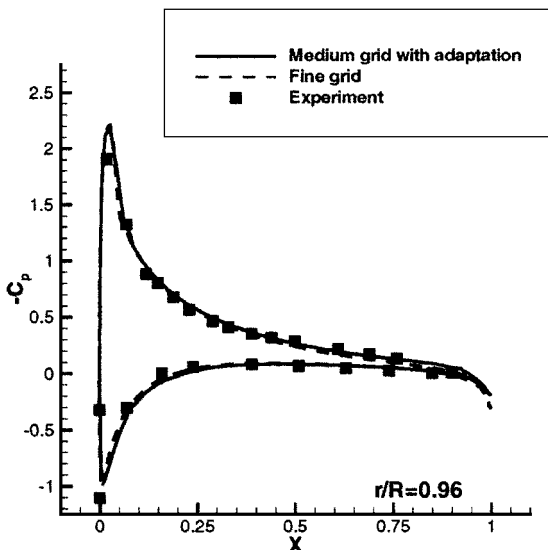
With respect to the adaptation frequency for time-accurate, time-periodic simulations, such as the simulation of a helicopter rotor in forward flight, two options exist: 1) simply adapt the grid at each implicit time step or 2) integrate the grid-adaptation sensor over a complete period, for example, corresponding to a user-specified azimuthal travel, and adapt the mesh based on this integrated sensor after the completion of the period. Both strategies have advantages and disadvantages. The first strategy is more efficient in terms of number of elements because elements are both created and removed at each implicit time step. Moreover, with the grid being adapted during the period, faster convergence to a periodic flow solution is achieved. However, since grid adaptation results in a dynamic load-balancing problem, for which currently no scalable algorithms are known, the parallel efficiency of the flow solver will deteriorate. The second strategy resembles the classical adaptation strategy used in steady-state problems. This method retains the parallel efficiency of the flow solver, but because the same adapted grid is used for all time steps, the number of elements is larger than in the first strategy. A compromise between the two grid-adaptation strategies is the following. At each implicit, time step the mesh is only refined based on the instantaneous grid-adaptation sensor and adaptation type. However, no elements are removed, as is done in the first strategy.



a)



b)



c)

Fig. 1 Surface pressure $-C_p$ distribution for the Caradonna-Tung helicopter rotor in hover (collective pitch angle, 12 deg, tip Mach number, 0.61; and Reynolds number, 2.7×10^6) compared with experimental data from Ref. 21 for radial stations r/R = a) 0.68, b) 0.89, and c) 0.96.

This effectively integrates the sensor in time and allows for faster convergence to the periodic flow solution. For the simulation of the helicopter rotor in forward flight presented in the next section, this compromise has been used.

Both adaptation strategies have their disadvantages. Either the number of elements is needlessly high, or a dynamic load-balancing problem is introduced. A new algorithm that does not suffer from these problems is presented by van der Ven.³⁰

Rotorcraft Simulations

Caradonna-Tung Helicopter Rotor in Hover

The standard Caradonna-Tung experiment has been conducted at NASA Ames Research Center and consists of a helicopter rotor in hover employing two cantilever-mounted, manually adjustable blades.²¹ Pressure transducers were located at five radial stations, namely, $r/R = 0.50, 0.68, 0.80, 0.89$ and 0.96 . The experiments were performed for collective settings of 0, 2, 5, 8, and 12 deg and angular velocities ranging from 650 to 2450 rpm.

The flowfield around the Caradonna-Tung helicopter rotor using a collective pitch setting of 12 deg and a tip Mach number of 0.61 has been simulated using the DG finite element method.

The multiblock grid generated at NLR of one-half of the computational domain consists of 55 blocks, with a total of 726,784 elements. Simulations have been performed on this so-called fine grid. In addition, simulations have been performed on a one-time coarser grid consisting of 90,848 elements (medium grid) with grid adaptation. After grid adaptation using the vortex sensor based on the vorticity in combination with uniformity sensor, the medium grid contains 135,280 elements. The grid in the vortex was adapted to a uniform mesh width equal to 0.1 chord lengths.

In Fig. 1, the surface pressure distribution at the three radial stations are compared with the experimental data.²¹ The agreement between the simulations and the experimental data is generally good. The pressure peak at the lower side of the rotor blade is resolved better on the fine grid. The results coincide very well with the experimental data at the lower side.

Figure 2 shows the sectional thrust for the medium grid with adaptation, the fine grid and the experiment.²¹ Both simulations show higher-than-measured thrust levels. The sectional thrust obtained on the fine grid is higher than the one obtained on the medium grid with adaptation, except for a small region near the rotor tip.

Figure 3 shows the vorticity contours at the 140-deg azimuth location behind the blade for the medium grid with grid adaptation and the fine grid. From these results, it can be seen that grid adaptation improves the vortex signature in terms of vorticity. Comparing these results with those presented by Raddatz and Rouzaud³¹ shows that the DG finite element method is able to carry vorticity over a longer distance and, thus, provides a clearer vortex signature.

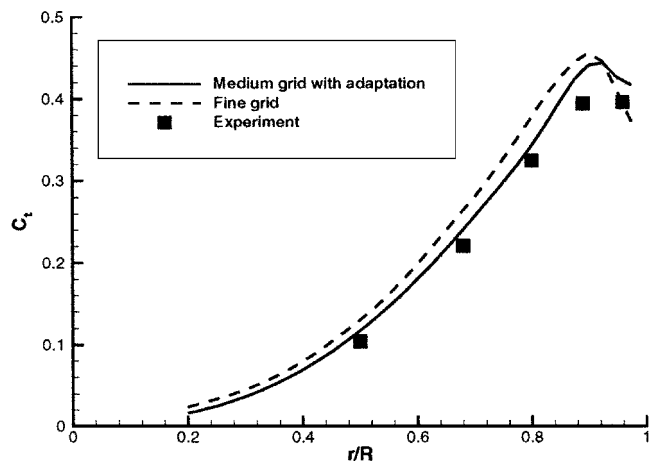


Fig. 2 Sectional thrust for the Caradonna-Tung helicopter rotor in hover for the medium grid with adaptation (135,280 elements), the fine grid (726,784 elements), and the experiment²¹ (collective pitch angle 12 deg and tip Mach number 0.61).

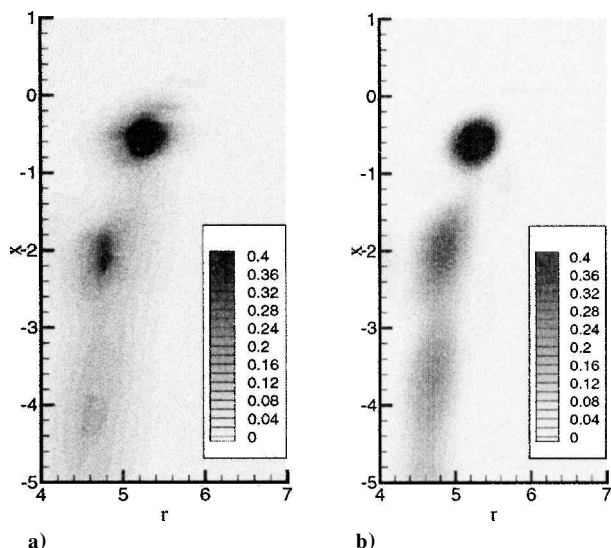


Fig. 3 Vorticity contours at the 140-deg azimuth location behind the blade for the Caradonna-Tung helicopter rotor in hover a) on the medium grid with adaptation (135,280 elements) and b) on the fine grid (726,784 elements, collective pitch angle 12 deg and tip Mach number 0.61).

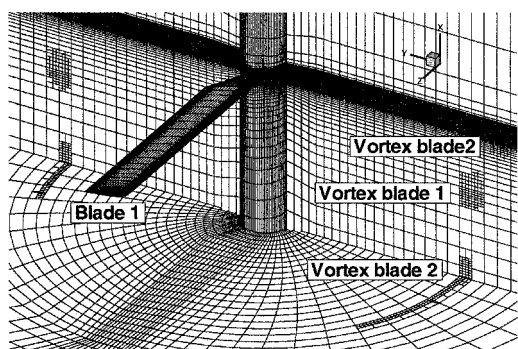


Fig. 4 Adapted Caradonna-Tung grid (135,280 elements) with periodic plane at $z = 0$ and plane at $x = -3.6$.

Note however, that the medium grid with grid adaptation consists of 135,280 elements with 20 degrees of freedom per element, resulting in a total of 2,705,600 degrees of freedom, which is almost twice as much as the 1,433,600 degrees of freedom reported by Raddatz and Rouzaud.³¹

The local behavior of the grid adaptation is presented in Fig. 4. Here, rotor blade 1, the periodic plane at $z = 0$, and the plane at $x = -3.6$ are shown. Clearly visible are the places where the vortex intersects these planes. At those positions one can see that the grid has been adapted to obtain a grid as isotropic and as uniform as possible in the vortex.

Figure 5 shows isocontours of the vorticity for the simulations on the fine grid. From Fig. 5, it is clear that the DG finite element method is able to capture the tip vortex over a distance of at least one-and-a-half revolution, provided the multigrid iterations are continued until all of the residuals of the 20 nonlinear algebraic equations per element are sufficiently converged. For the present simulations, a convergence of three orders was deemed sufficient. Note that the distance of one-and-a-half revolution equals the required distance for accurate blade-vortex interaction predictions. The convergence tolerance for the accurate capture of trailing vortices is, however, significantly tighter than the equivalent convergence tolerance needed to capture transonic shock waves.

Finally, Fig. 6 gives a quantitative comparison between the predicted and the experimental measured vortex trajectory up to an azimuth angle of 540 deg, that is, one-and-a-half revolutions behind the rotor blade. The agreement between the measured and the

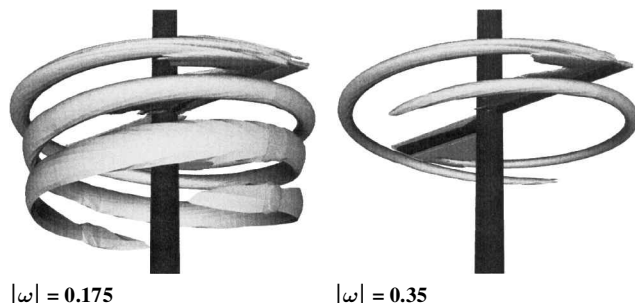


Fig. 5 Isocontour of the vorticity for the Caradonna-Tung helicopter rotor²¹ in hover on the fine grid (726,784 elements, collective pitch 12 deg, and $M_{tip} = 0.61$).

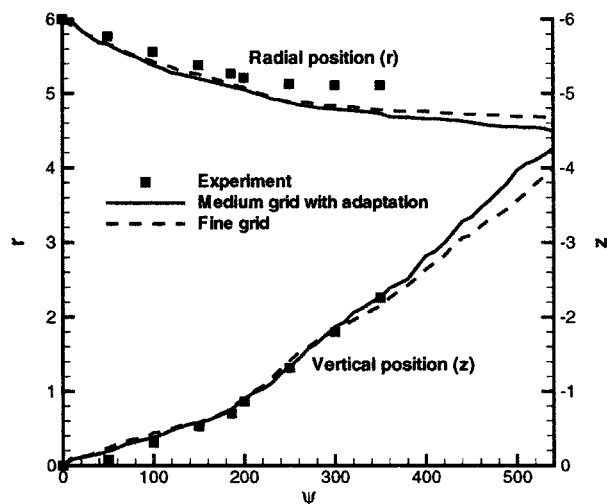


Fig. 6 Predicted and experimental vortex trajectory of the Caradonna-Tung rotor in hover on the medium grid with adaptation (135,280 elements) and on the fine grid (726,784 elements) with collective pitch angle 12 deg and tip Mach number 0.61; upper lines indicate radial position of the vortex and lower lines indicate vertical position of the vortex.

computed vertical position is good, except for the region close to the blade. The predicted radial contraction of the tip vortex shows reasonable agreement with the experimental data. The agreement between the simulation on the medium grid with adaptation and the fine grid is generally good.

The presented results, that is, the surface pressure distributions, the sectional thrust, and the vortex trajectories, are similar to the ones reported by Ahmad and Strawn,³² where the grid dependency of the rotor wake was studied for the case having a collective pitch setting of 8 deg and a tip Mach number of 0.439. Three different (background) grids having uniform mesh spacings were compared during this study.

OLS Helicopter Rotor Simulations

The capabilities of the DG flow solver with respect to the simulation of a helicopter rotor in forward flight have been tested against the OLS helicopter rotor experiment.³³ The OLS helicopter rotor corresponds to a $\frac{1}{7}$ -scale model of the AH-1 helicopter rotor. The planform of the AH-1G/OLS rotor is rectangular and the blade section equals a modified BHT-540 section. The airfoil has been modified to accommodate full-scale pressure instrumentation during the experiment. The resulting thickness is 9.71% of the chord length. The diameter of the rotor is 1.916 m and the chord length is 0.1039 m. The blades have a root cutout at 18.2% of the rotor radius. The rotor blades are twisted 10 deg from the blade root to the blade tip. In rest, the blade pitch angle at the 75% radial station is zero. All blade pitch angles are specified with respect to this station. The OLS helicopter rotor blades rotate about the quarter-chord.

The OLS helicopter rotor experiment has been conducted in the German–Dutch wind tunnel (DNW) to gather rotor-blade pressures and far-field radiated noise. At five radial stations, namely, $r/R = 0.75, 0.80, 0.85, 0.91$, and 0.975 , pressure transducers were located at the 3% chordwise station on both the upper and the lower side of the blade. The ranges of the four governing nondimensional parameters tested are 1) the tip Mach number $M_{tip} = 0.55$ – 0.72 , 2) the advance ratio $\mu = 0.13$ – 0.35 , 3) the thrust coefficient $C_T = 0.0047$ – 0.0080 , and 4) the tip-path plane angle $\alpha_{TPP} = -5$ – 7 deg.

The flowfield around the OLS helicopter rotor in forward flight has been simulated for the flow conditions of run 3020,³³ that is, a tip Mach number M_{tip} of 0.664 , an advance ratio μ of 0.164 , a thrust coefficient C_T of 0.0054 , and a tip-path plane angle α_{TPP} of 2 deg. This case correspondsto the following flight conditions: 1) a forward velocity of the rotor of 72 kn, that is, 37 m/s, and 2) a rate of descent of approximately 400 ft/min, that is, 2 m/s. The simulation has been performed on a multiblock grid generated at NLR consisting of 72 blocks with an initial total of $244,224$ elements.

The complete simulation consisted of several revolutions. A constant increment of the azimuth angle, that is, 1.25 deg, has been used. During the simulation the grid has been adapted twice. During the first adaptation (lasting half of a revolution) the vortex sensor based on the vorticity magnitude has been used in combination with the anisotropy sensor, resulting in a grid of $488,026$ elements. During the subsequent second adaptation (lasting one full revolution) the vortex sensor based on the vorticity magnitude has been used in combination with the uniformity sensor. The grid in the vortex was adapted to a uniform mesh width equal to 0.005 rotor diameters. At each implicit time step, the mesh has only been refined. Because no elements are removed, in this manner the vortex sensor is effectively integrated in time. After adaptation the grid contains $1,297,729$ elements.

Several settings for the blade motion coefficients have been used during the simulation. Two combinations of blade motion coefficients and computational grids will be shown here. First, on the grid consisting of $488,026$ elements, a simulation has been performed using the blade motion coefficients denoted as schedule 1 in Table 3. (No lead–lag schedule has been used.) Second, on the grid consisting of $1,297,729$ elements, a simulation using the blade motion coefficients denoted as schedule 2 in Table 3 has been performed. To obtain the pitch angles for this case, the already described trimming procedure using the complete sensitivity matrix for the pitch angles has been applied.

Figure 7 shows the differential pressure at the 3% chordwise station at $r/R = 0.975$ for these two cases. It can be seen that the result obtained using schedule 2 is significantly closer to the experiment than the result obtained using schedule 1. Although the effects of trimming and grid adaptation intertwine during these simulations, the overall improvement has been obtained by the trimming.

The obtained revolution-averaged thrust coefficient and rotor plane moment coefficients are shown in Table 4. Although the revolution-averaged thrust coefficient for schedule 2 is slightly

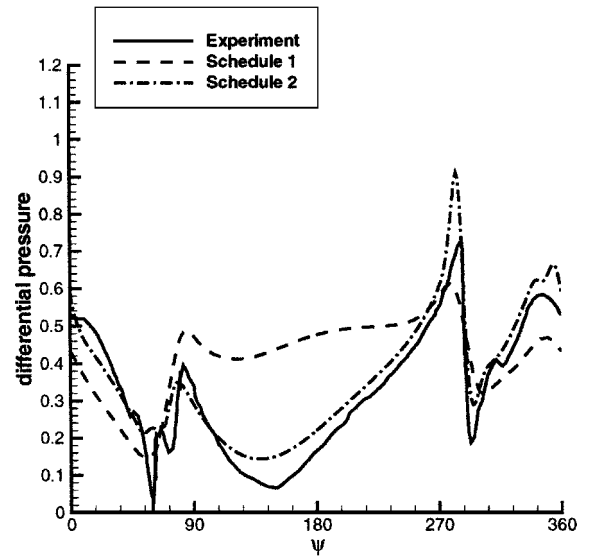


Fig. 7 Differential pressure $-\Delta C_p M^2$ at the 3% chordwise station at $r/R = 0.975$ for schedules 1 and 2 and the experiment (see Table 3).

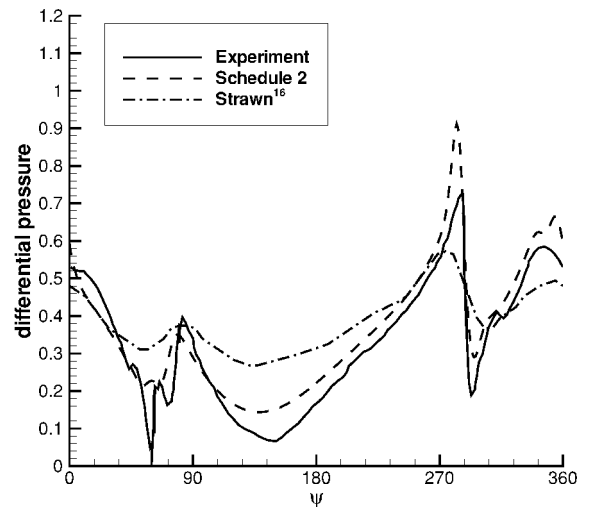


Fig. 8 Differential pressure $-\Delta C_p M^2$ at the 3% chordwise station at $r/R = 0.975$ for schedule 2, Strawn,¹⁶ and experiment.

higher than the experimental value of 0.0054 , the revolution-averaged rotor plane moment coefficients are small compared with those of schedule 1 and of Strawn.¹⁶ In Fig. 8, the differential pressure at the 3% chordwise station at $r/R = 0.975$ for schedule 2, Strawn,¹⁶ and the experiment are shown. Note that Strawn¹⁶ performed his simulations on a grid consisting of 1.8 million grid points and that during his simulation a constant increment of the azimuth angle of 0.25 deg was used.

In Fig. 9, the differential pressure at the 3% chordwise station for schedule 2 is compared with the experimental data obtained at the five radial stations, where pressure transducers were located. The agreement between the differential pressures obtained during the simulation and the experiment is generally good. As can be seen in Fig. 9, the overall agreement between the results obtained during the simulation and the experimental results improves with increasing radial position r/R . Several blade–vortex interaction events can be observed. When this Fig. 9 is compared with previously reported Euler and Navier–Stokes simulations for the OLS helicopter rotor in forward flight^{12,16} (see also Fig. 8), one can see that with the present method a considerable improvement has been obtained.

In Fig. 10, the sectional lift, the differential pressure at the 3% chordwise station, and the derivatives of the sectional lift and the differential pressure at that station with respect to the azimuth angle are shown. On both the advancing side and the retreating side, the

Table 3 Pitch and flap angles used in the OLS helicopter rotor simulation in forward flight

| Method | θ_0 , deg | θ_{1c} , deg | θ_{1s} , deg | β_0 , deg | β_{1c} , deg | β_{1s} , deg |
|----------------------|------------------|---------------------|---------------------|-----------------|--------------------|--------------------|
| Schedule 1 | 6.53 | 0.90 | −1.39 | 2.40 | −1.00 | 0.00 |
| Schedule 2 | 6.62 | 2.81 | −2.19 | 2.40 | −1.00 | 0.00 |
| Strawn ¹⁶ | 6.14 | 0.90 | −1.39 | 0.50 | −1.00 | 0.00 |

Table 4 Force and moment data from the OLS helicopter rotor simulation in forward flight

| Method | $C_T (\times 10^3)$ | $C_{Mx} (\times 10^3)$ | $C_{My} (\times 10^3)$ |
|-------------------------|---------------------|------------------------|------------------------|
| Experiment ^a | 5.40 | 0.00 | 0.00 |
| Schedule 1 | 5.440 | 0.161 | 0.519 |
| Schedule | 5.553 | 0.037 | −0.112 |
| Strawn ¹⁶ | 5.43 | 0.11 | 0.41 |

^aExperimental data is taken from Strawn.¹⁶

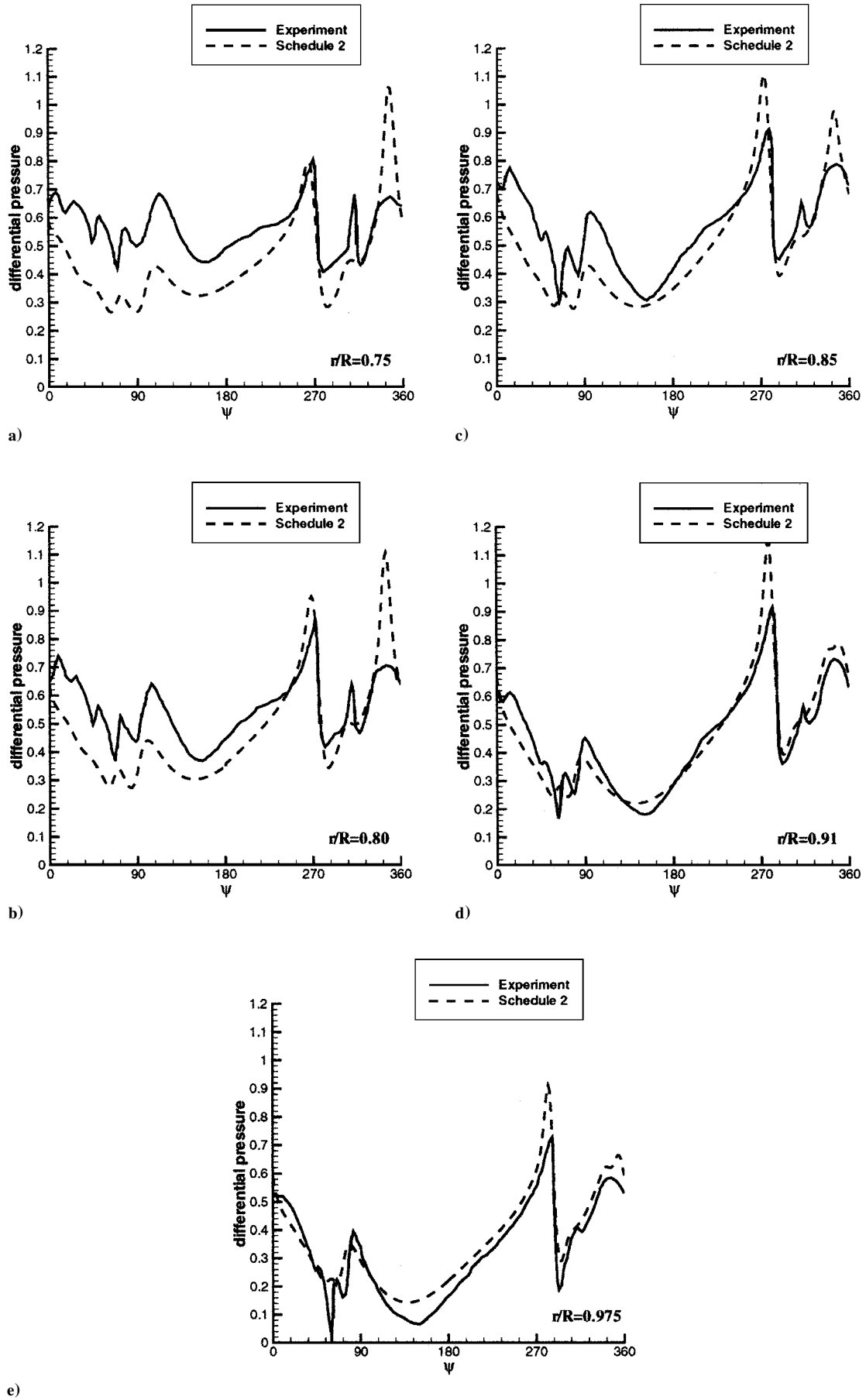


Fig. 9 Differential pressure $-\Delta C_p M^2$ at the 3% chordwise station for OLS helicopter rotor in forward flight at the radial stations r/R = a) 0.75, b) 0.80, c) 0.85, d) 0.91, and e) 0.975.

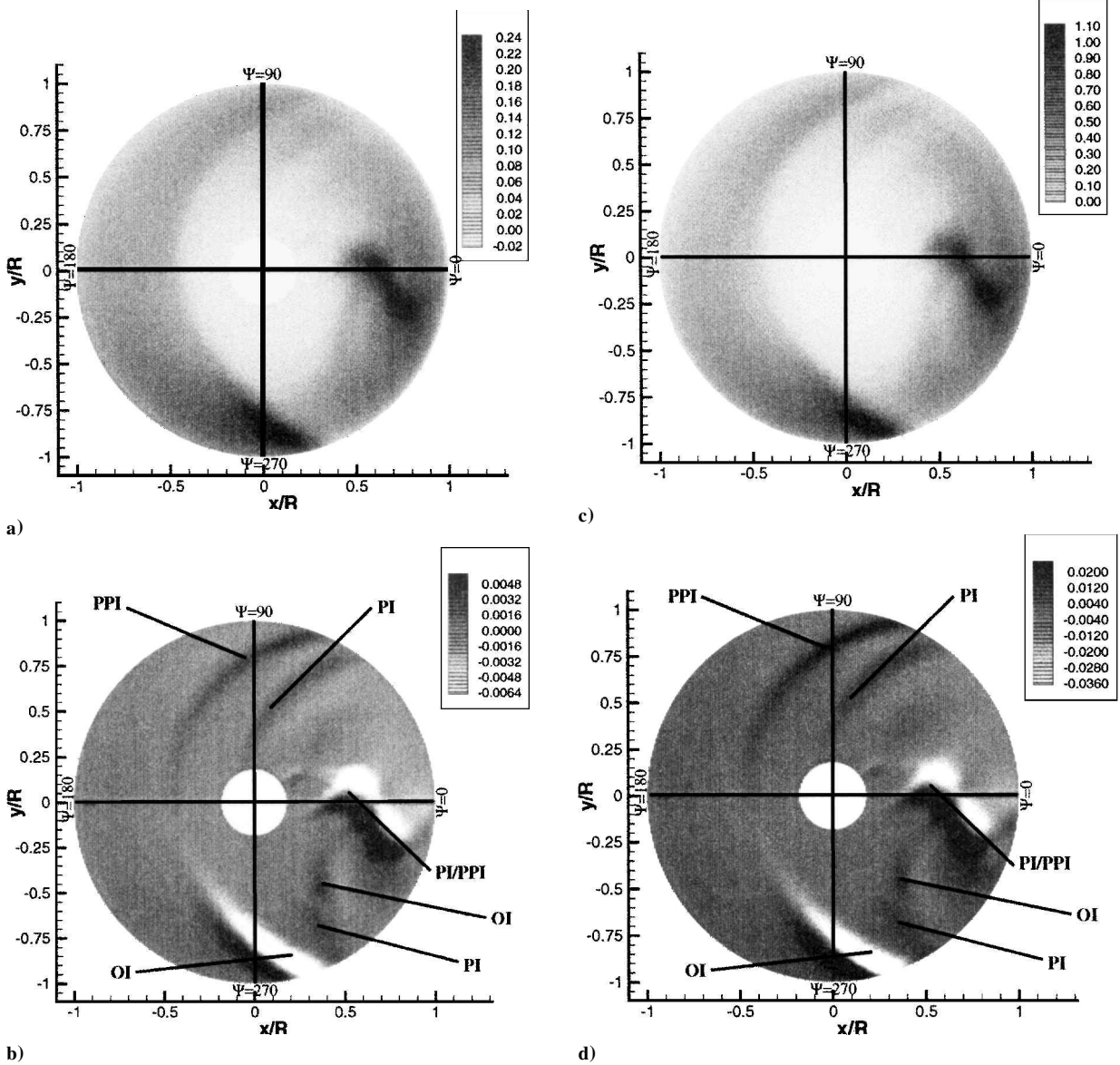


Fig. 10 Schedule 2 a) sectional lift, b) derivative of the sectional lift with respect to ψ , c) differential pressure $-\Delta C_p M^2$ at 3% chordwise station and d) derivative of the differential pressure $-\Delta C_p M^2$ at 3% chordwise station with respect to ψ .

present simulation finds two interactions. From $\psi = 0$ deg and looking in the counterclockwise direction, the rotor blade first interacts parallel with a vortex originating from the blade itself, next there is perpendicular interaction (PPI) with the vortex originating from the other blade, then there is once more an interaction with the vortex originating from the other blade which initially is perpendicular but develops into an oblique interaction (OI), and finally the blade interacts with a vortex originating from itself. This final interaction starts as a parallel interaction (PI), but develops into an OI. In Fig. 10, the effect of the root vortices can be clearly seen by the interactions around the zero azimuth angle. It is obvious that the presence of these vortices, which are not present in the experiment due to a different geometry in the hub region, influences the solution.

Review

The DG finite element algorithm based on a boundary-conforming ALE formulation in conjunction with unstructured grid refinement of hexahedral grids has been used for the simulation of rotor wake vortices.

The following simulations have demonstrated the simulation capabilities of this flow solver.

1) The Caradonna–Tung helicopter rotor in hover simulation has shown that this method is able to capture the tip vortex over a distance of at least one-and-a-half revolutions, both on a 726,784 element grid and a 135,280 element grid with local unstructured grid refinement.

2) The OLS helicopter rotor in forward flight simulation has shown the method's ability to perform time-accurate helicopter simulations on a single boundary-conforming grid.

All simulations showed that local grid adaptation, when applied, improves the vortex signature in terms of vorticity and/or helicity. Comparison with the experimental data is generally good. For the forward flight simulation, the rotor trimming procedure as developed at NLR has been used.

It was shown that, using this procedure, one obtains considerably improved results compared with previously reported Euler and Navier–Stokes simulations. These improvements are because all sensitivity coefficients with respect to the pitching parameters are used and because the sensitivity matrix is calculated using the Euler flow solver itself, instead of using a lifting line vortex method, such as CAMRAD/JA.²⁸

The presented DG method has the following features that make it well suited for the simulation of rotor wake flows.

1) The second-order accurate DG method carries the spatial flow-field gradients as explicit, dependent variables implying that the

vorticity is carried as a dependent flow variable; vorticity components are implicitly related to the three spatial gradients of the state vector (15 variables per element).

2) The algorithm allows degenerate, high-aspect-ratio elements near leading and trailing edges for efficiency.

3) The algorithm has an extremely compact stencil, and as a result, possesses an inherent ability to handle adaptive strategies because the refining and derefining of the elements (grid) is done without any need to consider special continuity requirements typical of conventional CFD methods.²⁶

4) The algorithm has an excellent parallelization potential because the communication between neighboring elements is strictly limited to the flow data exchange at common faces and will, therefore, be well suited for parallel computing platforms.

Furthermore, note that an extension of the DG algorithm from the Euler equations to the Navier–Stokes equations is feasible without compromising items 1–4, for example, see Atkins and Shu³⁴ for an analysis in two dimensions. With respect to vortex flow simulations, the main difference between a simulation using the Euler equations and a simulation using the Navier–Stokes equations is that for the former grid adaptation results in an unlimited increase of the vortex resolution.

Conclusions

The main issue explored in the present paper is the ability of the DG finite element approach to capture the tip vortex of a rotor over large distances (with and without grid adaptation). The conclusion is that the present DG algorithm can capture the tip vortex of a rotor in hover or forward flight over large distances, provided the multigrid iterations are continued until all of the residuals of the 20 nonlinear, algebraic equations per element are sufficiently converged. It is found that the convergence tolerance required for the accurate capture of trailing vortices is significantly tighter than the equivalent convergence tolerance needed to capture transonic shock waves, that is, transonic shock waves are easy to capture relative to the far-field signature of trailing vortices.

Comparison of results of the present DG method (with and without adaptation) with the results of more conventional algorithms^{12,13,16,31} shows that the present DG approach yields the same or better agreement between CFD and experimental data in terms of blade surface pressures, differential pressures, and vortex trajectories.

For accurate prediction of the flow around a rotor in forward flight, it was concluded that trimming of the rotor is of utmost importance. The trimming procedure developed at NLR resulted in substantially improved differential pressure distributions when compared with those presented in literature.^{12,13,16} Pahlke and Chelli¹³ remarked that “It was shown that the viscous effects are important for the prediction of the global forces but the effect of trim is even more important.” This remark stresses the aforementioned importance of proper trimming.

Acknowledgments

The authors would like to acknowledge the support of the Royal Netherlands Air Force (RNLAf Contract N98/19); The Boeing Company, Mesa; and the NLR. We would also like to thank J. van Muijden, S. P. Spekrijse, and H. A. Sytsma of National Aerospace Laboratory/NLR for making the grids and J. J. W. van der Vegt of the University of Twente, Enschede, The Netherlands, for his contributions to the discontinuous Galerkin finite element flow solver algorithm.

References

- ¹Boelens, O. J., van der Ven, H., Oskam, B., and Hassan, A. A., “Accurate and Efficient Vortex-Capturing for Rotor Blade-Vortex Interaction,” *AIAA Paper* 2000-0112, Jan. 2000.
- ²Boelens, O. J., van der Ven, H., Oskam, B., and Hassan, A. A., “Accurate and Efficient Vortex-Capturing for a Helicopter Rotor in Hover,” *26th European Rotorcraft Forum*, Sept. 2000.
- ³Boniface, J.-C., and Pahlke, K., “Calculations of Multibladed Rotors in Forward Flight Using 3D Euler Methods of DLR and ONERA,” *22nd European Rotorcraft Forum*, Sept. 1996.

- ⁴Bottasso, C. L., and Shephard, M. S., “Parallel Adaptive Finite Element Euler Flow Solver for Rotary Wing Aerodynamics,” *AIAA Journal*, Vol. 35, No. 6, 1997, pp. 937–944.
- ⁵Dindar, M., “An Adaptive Finite Element Procedure for Rotorcraft Aerodynamics and Aeroelasticity,” Rensselaer Polytechnic Inst., Troy, NY, 1998.
- ⁶Dindar, M., Shephard, M. S., Flaherty, J. E., and Jansen, K., “Adaptive CFD Analysis for Rotorcraft Aerodynamics,” *Computational Methods in Applied Mechanical Engineering*, Vol. 189, No. 4, 2000, pp. 1055–1076.
- ⁷Duque, E. P. N., and Srinivasan, G. R., “Numerical Simulations of a Hovering Rotor Using Embedded Grids,” *48th American Helicopter Society Annual Forum*, June 1992.
- ⁸Duque, E. P. N., Strawn, R. C., Ahmad, J., and Biswas, R., “An Overset Grid Navier–Stokes Kirchhoff-Surface Method for Rotorcraft Aeroacoustic Predictions,” *AIAA Paper* 96-0152, Jan. 1996.
- ⁹Hariharan, N., and Sankar, L. N., “A Review of Computational Techniques for Rotor Wake Modeling,” *AIAA Paper* 2000-0114, Jan. 2000.
- ¹⁰Kondo, N., Ochi, A., Nakamura, H., Aoyama, T., Saito, S., and Yamakawa, E., “Validation of Rotor Aerodynamic and Acoustic Prediction Methods Using ATIC 2nd Model Rotor,” *26th European Rotorcraft Forum*, Sept. 2000.
- ¹¹Ochi, A., Aoyama, T., Saito, S., Shima, E., and Yamakawa, E., “BVI Noise Predictions by Moving Overlapped Grid Method,” *55th American Helicopter Society Annual Forum*, May 1999.
- ¹²Pahlke, K., “Berechnung von Strömungsfeldern um Hubschrauberrotoren im Vorwärtsflug durch die Lösung der Euler-Gleichungen,” *Forschungsbericht 1999-22*, Deutsches Zentrum für Luft- und Raumfahrt e. V., 1999.
- ¹³Pahlke, K., and Chelli, E., “Calculation of Multiblade Rotors in Forward Flight Using a 3D Navier–Stokes Method,” *26th European Rotorcraft Forum*, Sept. 2000.
- ¹⁴Srinivasan, G. R., Baeder, J. D., Obayashi, S., and McCroskey, W. J., “Flowfield of a Lifting Rotor in Hover: A Navier–Stokes Simulation,” *AIAA Journal*, Vol. 30, No. 10, 1992, pp. 2371–2378.
- ¹⁵Strawn, R. C., Biswas, R., and Lyrantzis, A. S., “Helicopter Noise Predictions Using Kirchhoff Methods,” *Journal of Computational Acoustics*, Vol. 4, No. 3, Sept. 1996, pp. 321–339.
- ¹⁶Strawn, R. C., Ahmad, J., and Duque, E. P. N., “Rotorcraft Aeroacoustics Computations with Overset-Grid CFD Methods,” *54th American Helicopter Society Annual Forum*, May 1998.
- ¹⁷Strawn, R. C., and Ahmad, J., “Computational Modeling of Hovering Rotors and Wakes,” *AIAA Paper* 2000-0110, Jan. 2000.
- ¹⁸Webster, B. E., Shephard, M. S., Rusak, Z., and Flaherty, J. E., “Automated Adaptive Time-Discontinuous Finite Element Method for Unsteady Compressible Airfoil Aerodynamics,” *AIAA Journal*, Vol. 32, No. 4, 1994, pp. 748–757.
- ¹⁹Wissink, A. M., Lyrantzis, A. S., Strawn, R. C., Olikar, L., and Biswas, R., “Efficient Helicopter Aerodynamic and Aeroacoustic Predictions on Parallel Computers,” *AIAA Paper* 96-0153, Jan. 1996.
- ²⁰Yang, Z., Sankar, L., Smith, M., and Bauchau, O., “Recent Improvements to a Hybrid Method for Rotors in Forward Flight,” *AIAA Paper* 2000-0260, Jan. 2000.
- ²¹Caradonna, F. X., and Tung, C., “Experimental and Analytical Studies of a Model Helicopter Rotor in Hover,” *NASA TM* 81232, 1981.
- ²²Cockburn, B., “Discontinuous Galerkin Methods for Convection-Dominated Problems,” *High-Order Methods for Computational Physics*, edited by T. Barth and H. Deconinck, Lecture Notes in Computational Science and Engineering, Vol. 9, Springer-Verlag, Berlin, 1999, pp. 69–224.
- ²³Cockburn, B., Karniadakis, G., and Shu, C.-W., “An Overview of the Development of Discontinuous Galerkin Methods,” *Discontinuous Galerkin Methods, Theory, Computation and Application*, edited by B. Cockburn, G. E. Karniadakis and C.-W. Shu, Lecture Notes in Computational Science and Engineering, Vol. 11, Springer-Verlag, Berlin, 1999, pp. 3–50.
- ²⁴Van der Vegt, J. J. W., and van der Ven, H., “Discontinuous Galerkin Finite Element Method with Anisotropic Local Grid Refinement for Inviscid Compressible Flow,” *Journal of Computational Physics*, Vol. 141, No. 1, 1998, pp. 46–77.
- ²⁵Devine, K. D., and Flaherty, J. E., “Parallel Adaptive HP-Refinement Techniques for Conservation Laws,” *Applied Numerical Mathematics*, Vol. 20, No. 4, 1996, pp. 367–386.
- ²⁶Van der Vegt, J. J. W., and van der Ven, H., “Space-Time Discontinuous Galerkin Finite Element Method with Dynamic Grid Motion For Inviscid Compressible Flow. Part I. General Formulation,” *Journal of Computational Physics* (accepted for publication).
- ²⁷Van der Ven, H., and van der Vegt, J. J. W., “Accuracy, Resolution, and Computational Complexity of a Discontinuous Galerkin Finite Element Method,” *Discontinuous Galerkin Methods, Theory, Computation and Application*, edited by B. Cockburn, G. E. Karniadakis and C.-W. Shu, Lecture Notes in Computational Science and Engineering, Vol. 11, Springer-Verlag, Berlin, 1999, pp. 439–444.
- ²⁸Hassan, A. A., Charles, B. D., Tadghighi, H., and Burley, C., “A

Consistent Approach for Modeling the Aerodynamics of Self-Generated Rotor Blade–Vortex Interactions,” *Journal of the American Helicopter Society*, Vol. 41, No. 2, April 1996, pp. 74–84.

²⁹Caradonna, F. X., “Development and Challenges in Rotorcraft Aerodynamics,” AIAA Paper 2000-0109, Jan. 2000.

³⁰Van der Ven, H., Boelens, O. J., and Oskam, B., “Multitime Multigrid Convergence Acceleration for Periodic Problems with Future Applications to Rotor Simulations,” *International Parallel CFD 2001 Conference*, edited by Wilders et al., North-Holland Elsevier, Amsterdam, 2002, pp. 355–363.

³¹Raddatz, J., and Rouzaud, O., “Calculations of Multibladed Rotors in

Hover Using 3D Euler Methods of DLR and ONERA,” *21st European Rotorcraft Forum*, Paper II-6, Aug. 1995.

³²Ahmad, J. U., and Strawn, R. C., “Hovering Rotor and Wake Calculations with an Overset-Grid Navier–Stokes Solver,” *55th American Helicopter Society Annual Forum*, May 1999.

³³Boxwell, D. A., Schmitz, F. H., Spletstoesser, W. R. and Schultz, K. J., “Helicopter Model Rotor-Blade Vortex Interaction Impulsive Noise: Scalability and Parametric Variations,” *Journal of American Helicopter Society*, Vol. 32, No. 1, Jan. 1987, pp. 3–12.

³⁴Atkins, H. L., and Shu, C. W., “Analysis of the Discontinuous Galerkin Method to the Diffusion Operator,” AIAA Paper 99-3306, June 1999.